Dalton Transactions

ROYAL SOCIETY OF CHEMISTRY

PAPER

View Article Online
View Journal | View Issue

Cite this: *Dalton Trans.*, 2026, **55**, 2060

Engineering two-dimensional nanobranch architecture in PdAuAg for enhanced ethanol electrooxidation

Guangtao Wang,[a] Yuanyuan Min,[b] Ruiqi Shen,[a] Xuening Jin,[a] Yingying Wang,*[c] Yanyun Ma *[d] and Yiqun Zheng *[b]

We report a facile synthetic strategy for crafting unique trimetallic PdAuAg nanoplates with an abundant in-plane branching structure, termed "2D nanobranches". This distinctive architecture combines the benefits of a two-dimensional morphology with a highly dendritic, high-surface-area framework. Physicochemical characterization confirms the successful formation of the ternary alloy and the intricate branched structure. When assessed for the ethanol oxidation reaction (EOR) in an alkaline medium, the PdAuAg 2D nanobranches demonstrate enhanced specific activity, reaction kinetics, and cycling retention compared to a commercial Pd/C benchmark. *In situ* surface-enhanced Raman spectroscopy (SERS) reveals that the catalyst selectively promotes the C2 pathway for ethanol oxidation to acetic acid, with no detectable C–C bond cleavage, thereby elucidating the origin of its high operational efficiency. Furthermore, density functional theory (DFT) simulations suggest that a higher surface coverage of hydroxyl radicals (OH) in the alkaline environment makes a key reaction step in this pathway more energetically favorable. The enhanced performance is attributed to the synergistic interplay of the ternary composition, which modulates the electronic structure, and the unique 2D branched morphology, which provides a high density of active sites and facilitates mass transport. This work highlights the profound impact of morphological control in conjunction with multimetallic engineering for advancing electrocatalyst design.

Received 4th December 2025,
Accepted 2nd January 2026

DOI: 10.1039/d5dt02910d

rsc.li/dalton

1. Introduction

Two-dimensional (2D) noble metal nanostructures represent a sophisticated class of nanomaterials that have garnered significant interest in electrocatalysis.[1] These architectures uniquely combine the high surface area and planar geometry of 2D materials with the structural complexity and high density of active edges inherent to dendritic or branched morphologies.[2,3] Unlike simple nanoplates or nanoparticles, these intricate structures offer a dramatically increased number of low-coordinated atoms at their edges, corners, and kinks, which often serve as the primary active sites for catalytic reactions.[4–6] Furthermore, the in-plane branching with extended 2D framework facilitates efficient electron transport, while the branched, often porous, structure promotes superior mass transfer of reactants and products, making them exceptionally well-suited for electrochemical applications.[7–9]

The pursuit of such complex morphologies is driven by the limitations of conventional catalysts for critical reactions like the ethanol oxidation reaction (EOR), which is central to the operation of direct ethanol fuel cells.[10] The intrinsic sluggish kinetics of electrocatalysis and the severe catalyst poisoning by CO-like intermediates necessitate the development of advanced materials that go beyond simple composition or size control.[11–15] This is where the structural advantages of branched 2D nanostructures become paramount as their intricate network provides a vast and accessible surface area, effectively increasing the availability of active sites per unit mass of noble metal.[16,17] Moreover, the specific atomic arrangements at the branch tips and junctions can be particularly effective at manuevering the affinity of key intermediates, thereby enhancing catalytic durability and performance.[18–20]

From a synthetic perspective, achieving precise control over the in-plane growth of branches on a 2D noble metal scaffold is a complex challenge that relies on sophisticated crystal growth mechanisms.[21,22] The formation of such hierarchical

[a]*School of Resource & Environment and Safety Engineering, Jining University, Qufu, Shandong 273155, China*
[b]*School of Chemistry, Chemical Engineering, and Materials, Jining University, Qufu, Shandong 273155, China. E-mail: yzheng@jnxy.edu.cn*
[c]*Health Management Department, Shandong Vocational College of Light Industry, Zibo, Shandong 255300, China. E-mail: hxwyy2005@mail.sdu.edu.cn*
[d]*Institute of Functional Nano & Soft Materials (FUNSOM), Jiangsu Key Laboratory of Advanced Negative Carbon Technologies, Soochow University, Suzhou, Jiangsu 215123, China. E-mail: mayanyun@suda.edu.cn*

structures typically involves kinetic control over the nucleation and growth processes, often mediated by selective capping agents that promote anisotropic growth along specific crystallographic directions.[23] The introduction of a secondary or tertiary metal can further manipulate surface energies and growth rates, guiding the deposition of new atoms to form branches rather than allowing for layer-by-layer growth.[24] This intricate interplay between thermodynamic and kinetic factors is crucial for dictating the final architecture, branching density, and ultimately, the catalytic efficacy of the resulting material.[25]

Recent progress in synthesizing trimetallic PdAuAg nanocrystals has focused on achieving controlled shapes to optimize their catalytic and plasmonic properties. For instance, researchers have developed methods to produce core–shell structures,[26] alloyed nanoparticles,[27] and hollow or porous architectures[28] through galvanic replacement or co-reduction strategies. While these advances enable tuning of surface composition and strain, precise control over two-dimensional (2D) anisotropic growth in such ternary systems remains a significant challenge. In this context, our work introduces a distinct synthetic pathway using hexamethylenetetramine (HMTA) hydrolysis and halide-specific capping agents to direct growth. This method allows for the first-time realization of extended in-plane nanobranching within a 2D trimetallic PdAuAg system. This architecture uniquely combines the high surface area and low-coordination sites of dendritic growth with the efficient in-plane electron transport of a 2D template, a feature not accessible through existing methods for solid or 3D shapes.

The selection of Pd, Au, and Ag is grounded in d-band theory. Pd's high d-band center (~−1.8 eV) enables strong adsorption for C–C cleavage but also causes CO poisoning. Au and Ag have lower d-band centers (~−3.5 eV and ~−4.3 eV, respectively).[29] Their incorporation into a 2D structure electronically modulates surface Pd sites, shifting the local d-band center away from the Fermi level. This downshift optimally weakens the adsorption of poisoning intermediates like CO, thereby freeing active sites and enhancing both the activity and stability of the electrocatalyst for EOR.

The presence of hexamethylenetetramine (HMTA) was identified as a critical factor in directing the formation of the desired branched morphology. A combination of systematic characterization, electrochemical evaluation, and supporting density functional theory (DFT) calculations reveal that doping a palladium catalyst with gold and silver atoms lowers the energy barrier for the rate-determining step in the ethanol oxidation reaction (EOR), enhancing its catalytic performance.

2. Experimental details

2.1 Materials

Gold(III) chloride trihydrate ($HAuCl_4 \cdot 3H_2O$, 99.9%), sodium tetrachloropalladate(II) (Na_2PdCl_4, 98%), ascorbic acid (AA, 99.0%), hexadecyltrimethylammonium bromide (CTAB, 99%), hexadecyltrimethylammonium chloride (CTAC, 97%), octadecyltrimethylammonium chloride (OTAC, 98%), octadecyltrimethylammonium bromide (OTAB, 98.0%), hexamethylenetetramine (HMTA, ≥98.0%) were all obtained from Maclin Chemical (Shanghai, China) and used as received. Silver nitrate ($AgNO_3$, ≥99.8%) was obtained from SinoPharm (Shanghai, China) and used as received. Docosyltrimethylammonium chloride (DCTAC, 98%) were obtained from Kemeo Chemical (Tianjin, China) and used as received. In all experiments, we used deionized water with a resistivity of 18.2 MΩ cm, which was prepared using an ultrapure water system (Ulupure, China).

2.2 Standard procedure for the preparation of 2D PdAuAg NBs

In a typical procedure, an aqueous solution of octadecyltrimethylammonium chloride (OTAC, 1 mL, 200 mM) was mixed with deionized water (2.5 mL) in a 20 mL vial. Hexamethylenetetramine (HMTA, 100 mg) was added to the mixture and stirred until fully dissolved. The vial was then placed in an ice-water bath and stirred for 10 minutes to equilibrate the temperature. Subsequently, the metal precursors—hydrogen tetrachloroaurate(III) ($HAuCl_4$, 6 mL, 0.5 mM), silver nitrate ($AgNO_3$, 1.5 mL, 2 mM), and sodium tetrachloropalladate(II) (Na_2PdCl_4, 0.15 mL, 20 mM)—were introduced sequentially into the cold solution. Finally, L-ascorbic acid (AA, 1 mL, 10 mM) was injected as a reducing agent. The reaction vial was then transferred to a water bath maintained at 30 °C and left undisturbed for 30 minutes. The resulting nanostructures were collected by centrifugation, washed repeatedly with water, and re-dispersed in water for further characterization.

2.3 EOR measurements

EOR measurement was carried out in a standard three-electrode system controlled by a CHI-760E potentiostat (CHInstruments, China). Typically, a glassy-carbon electrode (3 mm in diameter), a Ag/AgCl electrode, and a Pt wire were used as the working-, reference-, and counter-electrode, respectively. The potential is converted using the eqn (1).

$$E_{(\mathrm{RHE})} = E_{(\mathrm{Ag/AgCl})} + 0.197 + 0.059 \times \mathrm{pH} \quad (1)$$

Prior to the electrocatalyst preparation, the as-prepared nanocrystals were washed to remove the residual surfactant for surface purification. Then, 1 mg (in terms of active metal mass) of as-prepared nanocrystals and 2 mg of carbon black were dispersed in 1 mL of water and vigorously sonicated for 30 min to form a uniform ink. Subsequently, 3 μL of the catalyst ink was drop-cast onto the glassy carbon electrode and dried naturally, followed by dropping 3 μL of Nafion solution (0.5%) and dried naturally. Prior to EOR measurements, electro-catalysts were first activated in nitrogen-saturated aqueous KOH solution (1 M) by CV cycling at a scan rate of 200 mV s^{-1} until the reproducible curves were obtained. CV curves in aqueous KOH solution (1 M) with or without ethanol (1 M) were then collected at 50 mV s^{-1}. Subsequent linear

sweep voltammetry (LSV) measurements were conducted in a 1 M KOH solution with 1 M ethanol at a scan rate of 10 mV s^{-1}. In the accelerated degradation test (ADT), cyclic voltammetry (CV) was performed continuously using a scan rate of 50 mV s^{-1}, with specific activity recorded after each set of 10 cycles until 100 cycles were completed.

The electrochemical active surface area (ECSA) was estimated from the charge associated with the reduction of the PdO monolayer. The reduction charge (Q_{PdO}) was integrated from the cathodic scan of the CV curve recorded in 1 M KOH. The ECSA was then calculated using the equation (eqn (2)):

$$\mathrm{ECSA} = \frac{Q_{\mathrm{PdO}}}{405\ \mu\mathrm{C\ cm^{-2}} \times m} \quad (2)$$

where m is the mass of Pd on the working electrode, and 405 μC cm^{-2} is the assumed charge for the reduction of a PdO monolayer.

Raman spectra were acquired on an inVia Reflex confocal Raman microscope (Renishaw, England) equipped with a 532 nm laser. The PdAuAg nanoplates were assembled into a spectroelectrochemical cell (ECR-200, Persertech) using the same electrodes and electrolyte as described above. Prior to testing, all solutions were purged with high-purity nitrogen for at least 30 minutes. Each spectrum was recorded with an exposure time of 50 s.

2.4 Instrumentations and characterizations

Transmission electron microscopy (TEM) images were acquired using an HT-7820 microscope (Hitachi) operating at an accelerating voltage of 120 kV. High-resolution TEM (HRTEM), high-angle annular dark-field scanning TEM (HAADF-STEM), and energy-dispersive X-ray spectroscopy (EDS)-STEM mapping were performed using a Talos F200X microscope (Thermo Fisher Scientific) operated at 200 kV. Scanning electron microscopy (SEM) imaging was performed using a Zeiss Ultra60 microscope operating at an accelerating voltage of 12 kV. The crystalline structures of the samples were characterized by X-ray diffraction (XRD) using a Rigaku MiniFlex600 diffractometer. Surface chemical states were analyzed by X-ray photoelectron spectroscopy (XPS) on a Thermo Fisher Scientific K-Alpha+ system with a monochromatic Al Kα source (1486.6 eV). The elemental composition was determined by inductively coupled plasma optical emission spectrometry (ICP-OES) using an ICAP-5000 spectrometer (Focused Photonics, China).

2.5 DFT simulation

All DFT calculations were performed using the CASTEP code.[30] We employed the Perdew–Burke–Ernzerhof (PBE) functional within the generalized gradient approximation (GGA) to describe exchange–correlation effects.[31] A plane-wave basis set with a cutoff energy of 450 eV was used. The surface was modeled using a four-layer $p(3 \times 3)$ slab, with the bottom two layers fixed during geometry optimization and a 15 Å vacuum layer to prevent inter-slab interactions. Integrations over the Brillouin zone utilized a 3 × 3 × 1 Monkhorst–Pack k-point grid. The reaction energy (E_r) is defined as: $E_r = E_{FS} - E_{IS}$, where E_{IS} and E_{FS} are the total energies of the initial and final states, respectively.

3. Results and discussion

3.1 Synthesis of 2D PdAuAg NBs

The synthesis and morphological evolution of the two-dimensional PdAuAg nanobranches are directed by a delicate balance of kinetics and templating effects, primarily governed by the self-assembly of octadecyltrimethylammonium (OTA^+) cations into lamellar micelles, as depicted in the proposed formation pathway (Fig. 1a). These micelles serve as an organic superstructure that templates inorganic growth by confining metal precursors and nascent nuclei within their hydrophilic interlayers, thereby initially promoting a two-dimensional, layer-by-layer growth mode that forms the initial plate-like structures (Fig. 1b). However, as deposition continues, the lattice mismatch and interfacial strain between the different metallic components accumulate. To relieve this strain, the atomic deposition at the edges of the 2D plates transitions from a smooth, layer-by-layer mode to a 2D island-like growth mode. This transition is analogous to a two-dimensional Stranski–Krastanov transition, where strain drives the formation of localized clusters on an existing 2D layer. These edge protrusions then act as preferential sites for rapid, anisotropic atomic addition, propagating in-plane to form the distinct nanobranches observed in Fig. 1c–e. The use of an ice-water bath is critical to moderate reduction kinetics, allowing this strain-driven morphological transition to occur in a controlled manner under the combined influence of lamellar templating and facet-specific capping. In short, the progression from confined plates to intricate 2D nanobranches can be understood as a strain-induced transition from 2D layer-by-layer to 2D island-like growth at the edges, orchestrated by the synergy among soft-template confinement, tailored reaction kinetics, and facet-specific control.

3.2 Structural characterizations of 2D PdAuAg NBs

The comprehensive morphological and structural analysis presented in Fig. 2 confirms the successful synthesis of two-dimensional, branched PdAuAg nanostructures with a specific strain profile. The SEM and TEM images (Fig. 2a–c) clearly illustrate the complex, anisotropic growth that leads to the well-defined nanobranch morphology, providing a high surface area crucial for catalytic applications. Based on statistical measurements of multiple particles, the average particle size was determined to be 59.66 ± 7.34 nm, with an average branch width of 6.13 ± 1.38 nm.

The HAADF-STEM image (Fig. 2d) and the corresponding EDX elemental mapping (Fig. 2e) reveal a critical finding: the homogeneous distribution of Pd, Au, and Ag throughout the nanobranches. This indicates the formation of a solid-solution alloy, rather than a phase-segregated or core–shell structure. The EDS analysis confirms a Pd/Au/Ag atomic ratio of approximately 1 : 1 : 1, which aligns closely with the precursor stoi-

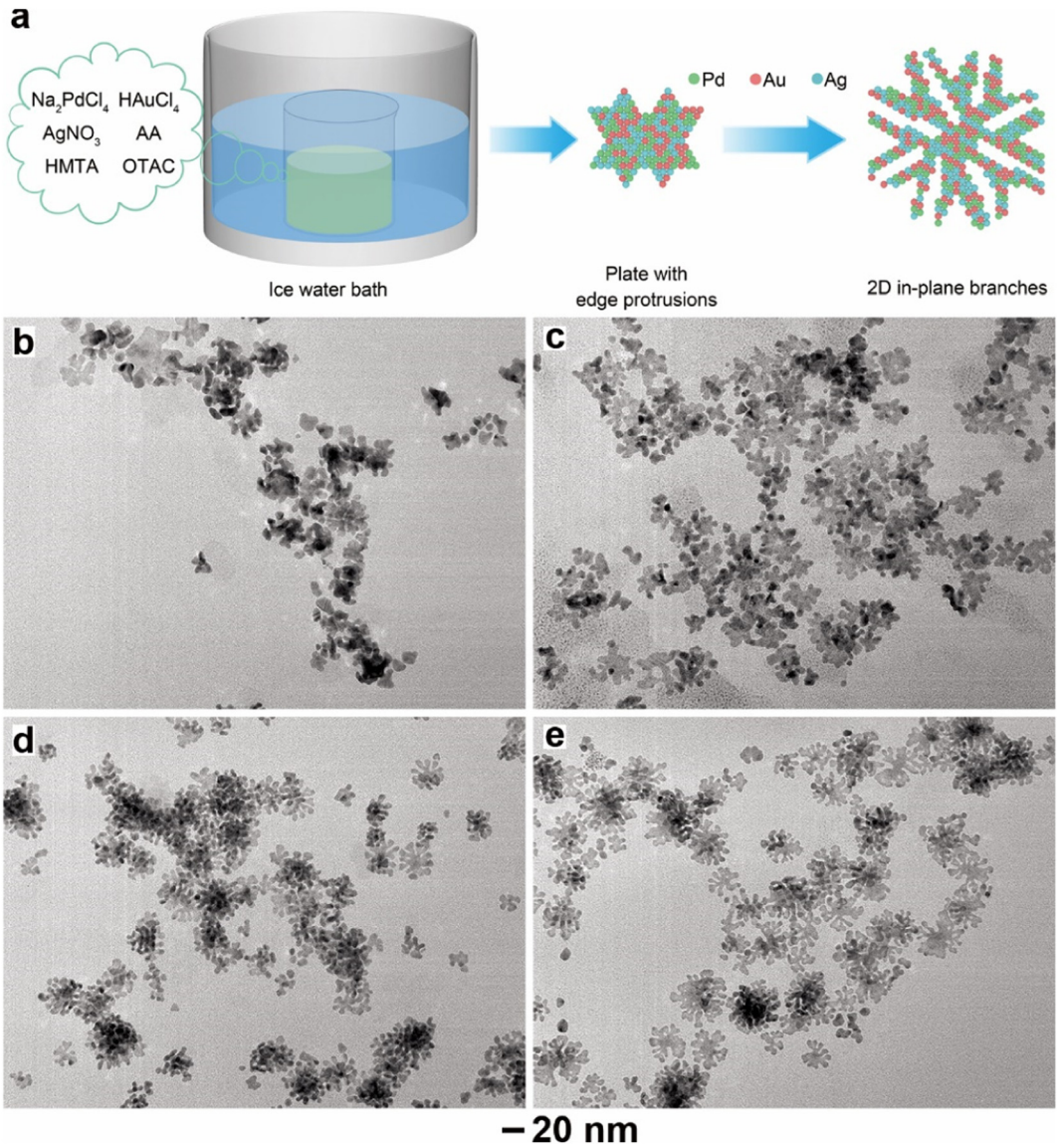

Fig. 1 (a) Schematic illustration of the formation process of 2D PdAuAg nanobranches. (b–e) TEM images of the nanostructures obtained by systematically reducing the molar amounts of Pd, Au, and Ag precursors to (b) 1/20, (c) 1/10, (d) 1/5, and (e) 1/2 of the standard group.

chiometry and indicates successful co-reduction of the metals (Fig. S1). The HRTEM image (Fig. 2f) shows clear lattice fringes with a measured interplanar spacing of 0.23 nm. The polycrystalline nature of the nanobranch is unequivocally demonstrated by the ring-like pattern with multiple spots in the Fast Fourier Transform (FFT) (inset, Fig. 2f). This suggests that the branches are composed of numerous small, randomly oriented crystalline domains. The identified lattice spacing of 0.23 nm lies between the standard values for the {111} planes of pure Pd (0.225 nm), Au (0.235 nm), and Ag (0.236 nm). This deviation from the parent metals is a direct consequence of the alloying effect, where the atomic radii of the constituent elements lead to a lattice contraction or expansion.

Most notably, the Geometric Phase Analysis (GPA) in Fig. 2g and h provides a direct visualization of the strain state within the nanobranches. The maps for the ε_{xx} and ε_{yy} strain components both confirm a pervasive compressive strain in the plane of the nanostructure. This compressive strain can be rationally attributed to the incorporation of the smaller Pd atoms (atomic radius ~137 pm) into the lattice of the larger Au (~144 pm) and Ag (~144 pm) atoms. The lattice mismatch introduces a structural constraint, compressing the crystal lattice.

As shown in Fig. S2, the XRD pattern exhibits a series of diffraction peaks positioned between those of the face-centered cubic (fcc) standards for pure Pd, Au, and Ag, indicating the formation of a homogeneous ternary alloy rather than a simple mixture of individual metals or core–shell structures. Notably, the absence of separate peaks for the constituent metals and the slight shift of the primary peaks from their

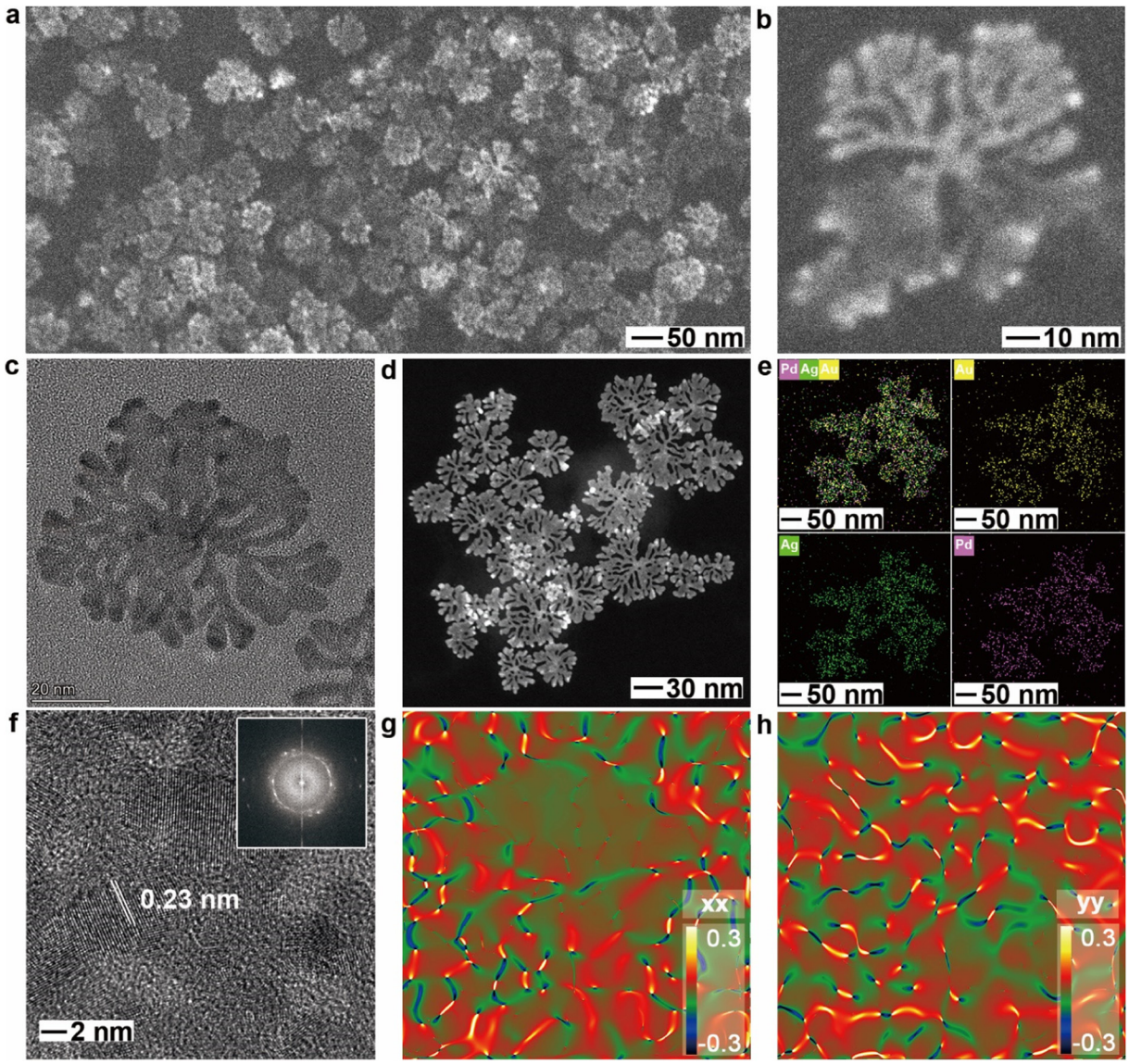

Fig. 2 Morphological and structural characterization of 2D PdAuAg nanobranches. (a and b) SEM images at different magnifications. (c) TEM image. (d) HAADF-STEM image. (e) Corresponding EDX elemental mapping showing the distribution of Pd (pink), Au (yellow), and Ag (green). (f) HRTEM image; the inset shows the Fast Fourier Transform (FFT) pattern. (g and h) Geometric phase analysis (GPA) strain maps of the ε_{xx} and ε_{yy} components, respectively.

standard positions suggest significant lattice integration, likely resulting from the concurrent reduction and co-deposition process under kinetic control.

To support this, we calculated the lattice parameter from the XRD data (~4.058 Å), which is very close to the theoretical value predicted by Vegard's law for a 1 : 1 : 1 PdAuAg alloy (~4.018 Å). This close agreement (a difference of only ~0.04 Å, or about 1%) strongly validates the formation of a homogeneous ternary alloy rather than a mixture of separate metallic phases (Table S1). Moreover, the peak broadening is a hallmark of nanoscale crystallite dimensions. Applying the Scherrer equation to the (111) peak reveals an average crystallite size of approximately 18.7 nm. This size is close to the width of the primary nanobranches observed in TEM images, confirming that the hierarchical structures are composed of ultrafine crystalline domains.

Complementing the XRD findings, the high-resolution XPS spectra provide critical insight into the surface composition and electronic interactions within the alloy. The XPS analysis of the 2D PdAuAg nanobranches (Fig. S3 and Table S2) confirms the presence of all three metals, each exhibiting a mixed oxidation state. The data reveal metallic Au(0) (B.E. 82.89, 86.63 eV) and Ag(0) (B.E. 367.25, 373.27 eV) as dominant species, co-existing with their surface-oxidized states Au(I) (83.66, 87.53 eV) and Ag(I) (368.15, 374.17 eV). Notably, Pd displays a substantial oxidized component, with Pd(II) peaks (334.40, 340.52 eV) of comparable intensity to the metallic Pd (0) signals (335.56, 339.74 eV). This uniform presence of

surface oxides, particularly the prominent Pd(II), is attributed to the high surface reactivity of the branched morphology.

The pronounced oxide signature in the XPS spectra is indeed a characteristic feature of our 2D branching nanostructures, stemming from their intrinsic material properties. This observation is attributed to two synergistic factors: (i) the limited thickness and high surface-to-volume ratio of the branched architecture ensure a dominant population of under-coordinated surface atoms, which are highly reactive and prone to oxidation, even under ultra-high vacuum conditions; (ii) the oxophilic nature of Pd, a key constituent, provides a strong thermodynamic driving force for the formation of stable sub-stoichiometric surface oxides (*e.g.*, PdO_x, $x < 1$). Therefore, the oxide signals reflect the authentic surface chemical state of the nanocrystals rather than mere adventitious contamination.

3.3 Influence of synthetic parameters on product morphology

The morphological evolution of the product as a function of HMTA concentration is presented in Fig. 3. The absence of HMTA resulted in the formation of uncracked nanoplates (Fig. 3a). In contrast, the introduction of HMTA invariably led to the formation of 2D nanobranches, with the branch length and cracking density being directly dependent on the HMTA concentration (Fig. 3b–f). This morphological transition is governed by the hydrolysis products of HMTA, namely NH_3 and HCHO.[32] Ammonia serves a dual purpose: it regulates solution pH to control the speciation and reduction kinetics of ascorbic acid (AA), while also forming stable $[M(NH_3)_4]^+$ complexes (M = Pd, Au, Ag) that increase the activation barrier for reduction, thereby slowing metal deposition. Concurrently, HCHO functions as a mild reducing agent, maintaining a controlled electron supply under alkaline conditions to facilitate branched growth.[33]

The influence of surfactant structure on product morphology is summarized in Fig. S4. A comparison between OTAB and OTAC isolates the role of the anion under identical lamellar confinement imposed by the OTA^+ cation. Br^- in OTAB binds strongly and isotropically to Au surfaces,[34–36] poisoning active sites and restricting growth, which yields short-branched nanostructures (Fig. S4a). In contrast, Cl^- in OTAC exhibits weaker and less specific adsorption, permitting greater adatom mobility and sustained 2D extension within the lamellar template, leading to longer nanobranches. Replacing OTAC with BTAC while retaining Cl^- produces nanoplates with stunted protrusions (Fig. S4b), as the rigid benzyl headgroup stabilizes basal planes through π-interactions but suppresses edge reorganization. Conversely, CTAC—with the same Cl^- anion but a shorter alkyl chain—also enables 2D nanobranch growth, yet the branches remain short, likely due to reduced micellar stability that limits prolonged elongation (Fig. S4c). This anion-dependent trend is further highlighted when CTAB replaces CTAC: the strongly adsorbing Br^- induces isotropic 3D dendritic growth (Fig. S4d) by poisoning anisotropic sites and disrupting 2D templating, promoting multidirectional nucleation. In short, morphology is governed predominantly by counterion chemistry (Br^- *vs.* Cl^-), while surfac-

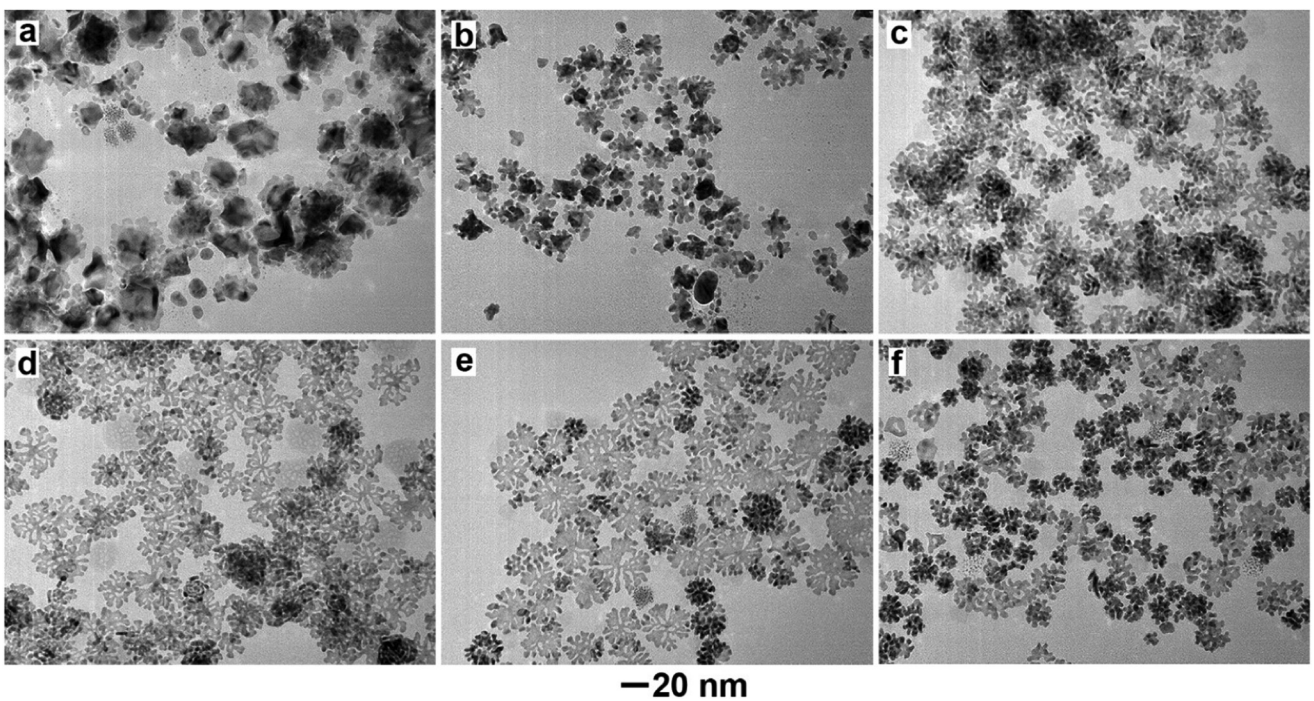

Fig. 3 Effect of hexamethylenetetramine (HMTA) amount on product morphology. TEM images of the products synthesized using different amounts of HMTA: (a) 0 mg, (b) 10 mg, (c) 20 mg, (d) 50 mg, (e) 200 mg, and (f) 500 mg. All other synthesis parameters were held constant.

tant chain length and headgroup structure modulate micellar confinement and stability rather than directly controlling product elongation.

3.4 EOR performance of 2D PdAuAg NBs

The electrochemical data presented in Fig. 4 suggest that the carbon-supported 2D PdAuAg nanobranches (NBs) exhibit promising performance for the ethanol oxidation reaction (EOR) when compared to a commercial Pd/C benchmark. Analysis of the cyclic voltammetry in the base electrolyte (Fig. 4a) indicates a lower electrochemical active surface area (ECSA) for the 2D PdAuAg NBs/C (159.4 cm^2 mg_{Pd}^{-1}) relative to Pd/C (368.7 mg_{Pd}^{-1}). This difference in ECSA might be partly due to the nanobranch morphology, where some degree of re-stacking could reduce the surface area accessible for electrochemical measurement, despite the material's inherent complexity.

Interestingly, as shown in the CV curves in Fig. 4b, the 2D PdAuAg NBs/C demonstrates a higher specific activity in the ethanol-containing electrolyte (1.25 mA cm^{-2}) compared to Pd/C (0.52 mA cm^{-2}). This observation suggests that the ternary composition could offer a more favorable electronic environment for EOR on a per-active-site basis (Fig. 4c). This trend toward enhanced intrinsic activity appears supported by the lower onset potential observed in the LSV profiles (317 mV, Fig. 4d) and the smaller Tafel slope from kinetic analysis (171.5 mV dec^{-1}, Fig. 4e), both of which are consistent with improved reaction kinetics.

Furthermore, as shown in Fig. 4f, the 2D PdAuAg NBs/C catalyst shows encouraging stability over 100 cycles, with a less pronounced degradation in peak current density compared to Pd/C. This improved durability aligns with the lower j_p/j'_p ratio observed for the ternary catalyst (0.24 *vs.* 2.26 for Pd/C), which may indicate a reduced tendency for the catalyst surface to accumulate poisoning intermediates. Taken together, these electrochemical results point toward the potential of the 2D PdAuAg NBs/C architecture, where the benefits of its ternary composition—including enhanced specific activity, favorable kinetics, and improved stability—appear to compensate for its lower electrochemical surface area (Table S3).

The unique in-plane branched architecture offers distinct advantages for the EOR over other anisotropic morphologies. Compared to solid nanoplates, which offer limited edge sites and tend to stack,[37] our branched structures expose a significantly higher density of low-coordination atomic sites along the numerous branch edges and junctions—key active centers for breaking the C–C bond in ethanol. Furthermore, unlike 3D dendritic structures where mass transport and electron conduction can be hindered by tortuous pathways, our 2D-confined, open-branch network ensures efficient electron transport along the conductive template and unimpeded access of reactants to active sites. This design also confers greater structural stability, as the branches are anchored to a central core,

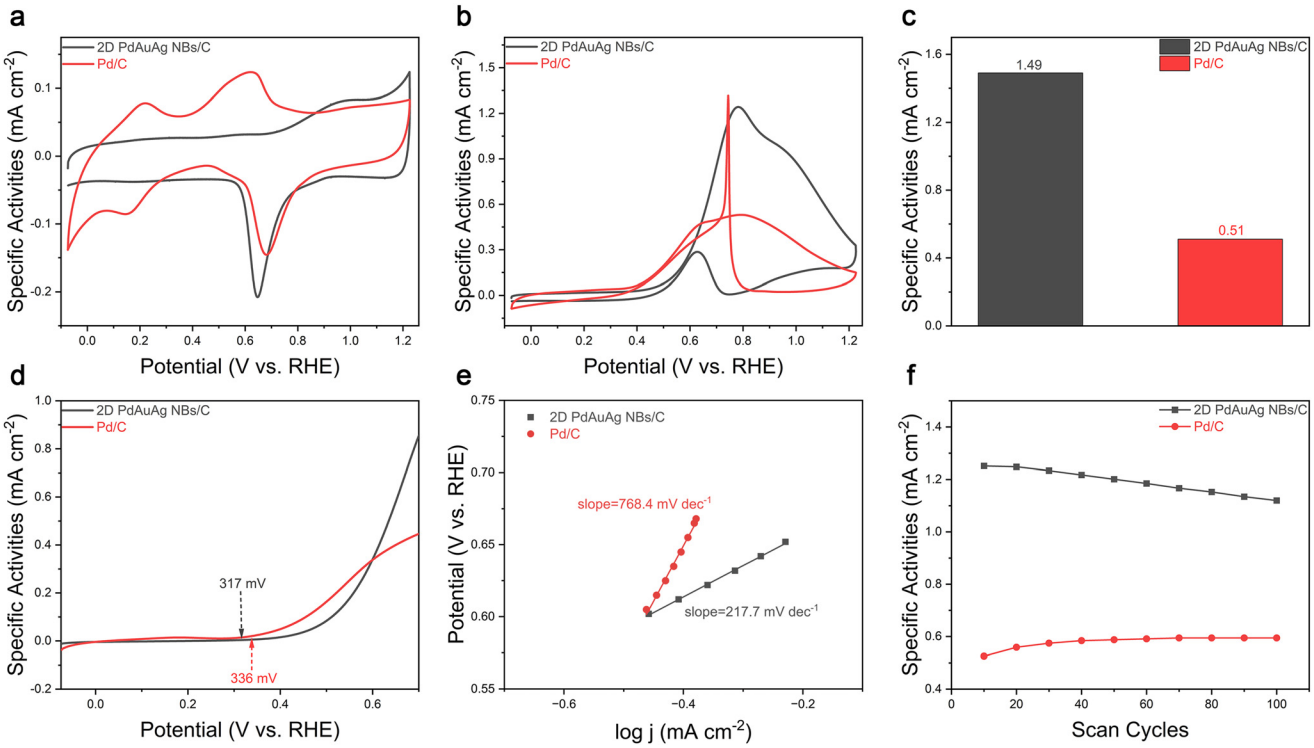

Fig. 4 EOR results: (a) cyclic voltammograms (CVs) in 1 M KOH, (b) CVs in 1 M KOH with 1 M ethanol, (c) histogram comparing the specific activities, (d) linear sweep voltammetry (LSV) for ethanol oxidation, (e) corresponding Tafel plots, and (f) stability test over 100 cycles at a scan rate of 50 mV s^{-1}.

mitigating the aggregation common to nanoplates or the degradation of fragile dendritic tips under operational potentials.

3.5 Insights from *in situ* Raman analysis

The *in situ* surface-enhanced Raman spectroscopy (SERS) analysis of the 2D PdAuAg nanobranches during ethanol electrooxidation provides a detailed view of catalyst activation and the reaction pathway (Fig. 5a). The initial spectra are dominated by fundamental ethanol vibrations. A distinct peak at ~1535 cm^{-1}, attributed to the OTA capping agent, is prominent at low potentials but weakens significantly after 0.5 V (Fig. 5b), indicating the potential-driven desorption of this surfactant to reveal the active sites.

The formation of the C2 oxidation product, acetic acid/acetate, is clearly tracked by key vibrational bands (Fig. 5c). The C═O stretching vibration at ~1640 cm^{-1} appears early and maintains a strong intensity, indicating a persistent carbonyl intermediate. The subsequent and parallel intensification of the peaks at ~927 cm^{-1} and ~1415 cm^{-1}, characteristic of acetic acid and the O–C–O stretching of acetate respectively, confirms the potential-dependent formation and accumulation of the final acid product, particularly after 0.8 V.

The consistent absence of a carbon monoxide (CO) adsorption band across the potential range rules out significant C–C bond cleavage. Therefore, the spectral evolution demonstrates that the 2D PdAuAg nanobranches selectively facilitate the complete C2 pathway for ethanol oxidation to acetic acid, a process initiated by surfactant desorption and culminating in the potential-dependent formation of the acid.

3.6 Insights from DFT simulations

To elucidate the enhanced EOR performance resulting from Au and Ag atom doping, DFT calculations were performed. Two representative surface models—Pd(111) and AuAgPd (111)—were constructed. It is well established that EOR on metal surfaces in alkaline media proceeds through multiple reaction steps, with acetate being the primary product.[38,39] Moreover, hydroxyl radicals (OH) have been shown to play a critical role in the EOR activity of Pd-based catalysts, as adsorbed OH species facilitate the oxidation of carbonaceous intermediates generated during the reaction.[40] Therefore, our study focuses on the oxidation pathway of CH_3CH_2OH to CH_3COOH in the presence of adsorbed OH on Pd-based catalysts. We examined key intermediates involved in the EOR mechanism on both Pd(111) and AuAgPd(111) surfaces, which include species from the dehydrogenation steps: CH_3CH_2OH, CH_3CH_2O, CH_3CHO, and CH_3CHOOH (Fig. 6a and b). Based on these intermediates, the energy barriers associated with CH_3COOH formation were evaluated for both catalysts (Fig. 6c and d). Among the elementary steps in the EOR pathway, the rate-determining step is identified as the formation of CH_3CHO from CH_3CH_2O and adsorbed OH. The activation energy for this step is lower on AuAgPd(111) (0.47 eV) than on Pd(111) (0.58 eV), indicating that the AuAgPd(111) model catalyst exhibits superior EOR catalytic performance.

To further understand the catalytic activity of both models, the projected density of states (PDOS) of surface Pd atoms was analyzed (Fig. 6e). The d-band center of AuAgPd(111) (−2.18 eV) was found to be closer to the Fermi level compared to that of Pd(111) (−2.45 eV). This result indicates that the incorpor-

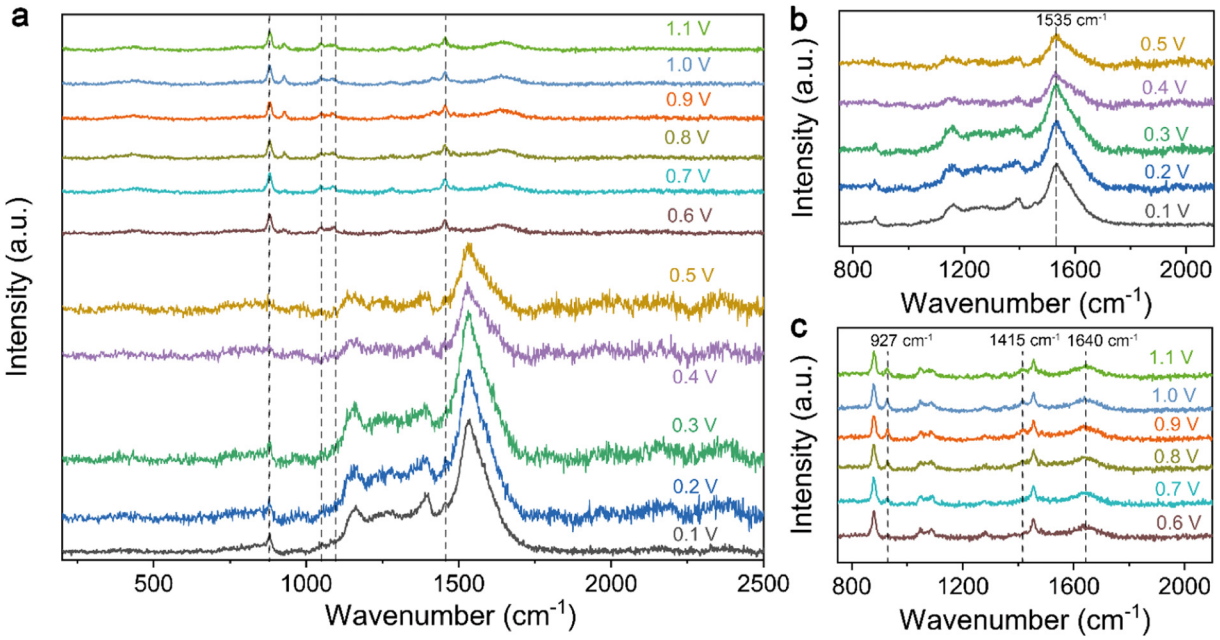

Fig. 5 *In situ* SERS analysis of the EOR mechanism on 2D PdAuAg nanobranches. (a) Time-series SERS spectra collected during chronoamperometry at various applied potentials (*vs.* RHE). (b and c) Selected spectra from key spectral regions.

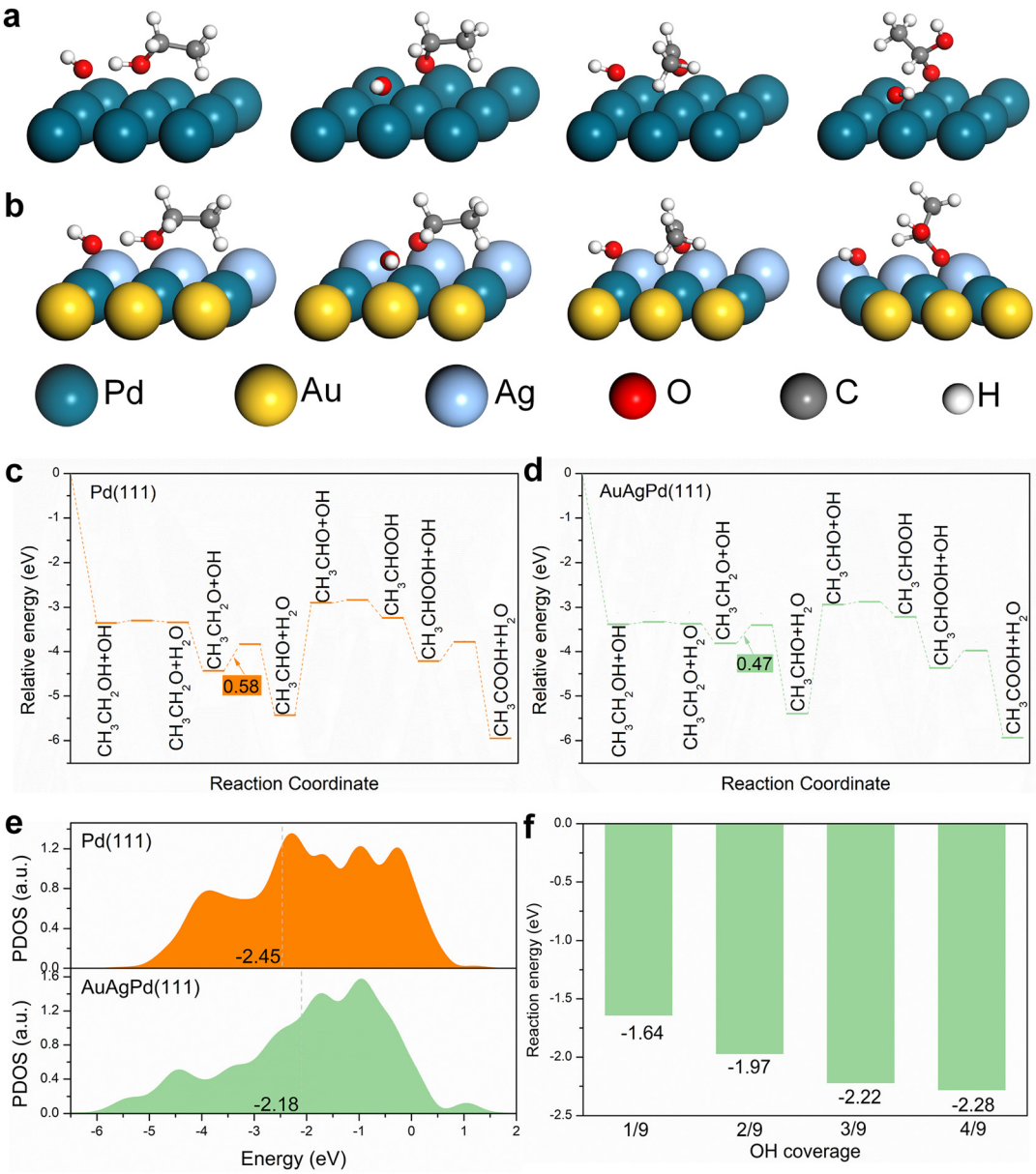

Fig. 6 DFT calculation results. Optimized adsorbate structures on (a) Pd(111) and (b) AuAgPd(111). Reaction energy profiles on (c) Pd(111) and (d) AuAgPd(111). (e) PDOS for Pd d-band center on Pd(111) and AuAgPd(111). The Fermi level is set to 0 eV, and the d-band center for each surface is indicated by a gray dashed line. (f) Reaction energy of CH_3CHO formation step at different OH coverage on AuAgPd(111) surface.

ation of Au and Ag atoms induces an upshift of the Pd d-band center. The electronic perturbation caused by alloying likely strengthens the interaction between active sites and adsorbates, thereby enhancing the catalytic activity toward EOR. To understand the influence of the alkaline environment, we assessed how OH surface coverage modulates CH_3CHO formation on AuAgPd(111) surface. As shown in Fig. 6f, the reaction energy for this step became more favorable with increasing coverage, decreasing from −1.64 eV at 1/9 ML to −2.28 eV at 4/9 ML. This demonstrates that higher OH coverage lowers the reaction energy for CH_3CHO formation, thereby enhancing the catalytic properties for EOR.

4. Conclusions

In conclusion, we have successfully demonstrated the synthesis of trimetallic PdAuAg 2D nanobranches as a superior electrocatalyst for the ethanol oxidation reaction. The unique in-plane branching architecture within a two-dimensional framework was found to be pivotal, providing a high density of accessible active sites and facilitating efficient mass transport. Combined with the synergistic electronic effect of the ternary PdAuAg alloy, which optimizes the adsorption of reactive intermediates and enhances anti-poisoning capability, this catalyst achieves enhanced electrocatalytic performance, including

higher mass activity and better long-term stability compared to commercial Pd/C catalysts. The improved activity, as verified by DFT simulations, could be attributed to an electronic effect, where the incorporation of Au and Ag shifts the Pd d-band center closer to the Fermi level, strengthening the interaction with key reaction intermediates. These findings underscore the profound benefits of integrating precise morphological control with multimetallic synergy for advanced electrocatalyst design.

Conflicts of interest

The authors declare that they have no known competing financial interests or personal relationships that could have appeared to influence the work reported in this paper.

Data availability

The data supporting this article have been included as part of the supplementary information (SI). Brief description: EDS pattern; XRD and XPS data for material characterization; TEM images from control experiments; a summarized table of ethanol oxidation reaction (EOR) performance metrics. See DOI: https://doi.org/10.1039/d5dt02910d.

Acknowledgements

This work was financially supported by the Shandong Provincial Natural Science Foundation (grant no. ZR2022MB120 & ZR2025QC109), the Hundred Outstanding Talent Program of Jining University (grant no. 2020ZYRC05 & 2023ZYRC9), and the Science and Technology Innovation Team Foundation of Jining University (no. 23KCTD04 & 23KCTD05&24KCTD09).

This work is also supported by the University Feature Laboratory for Energy Conversion and Nanocatalysis of Shandong Province, the Suzhou Key Laboratory of Functional Nano & Soft Materials, the Collaborative Innovation Center of Suzhou Nano Science & Technology, the 111 Project, and the Joint International Research Laboratory of Carbon-Based Functional Materials and Devices.

References

1 S. Yu, C. Zhang and H. Yang, *Chem. Rev.*, 2023, **123**, 3443–3492.
2 Y. Chen, Z. Fan, Z. Zhang, W. Niu, C. Li, N. Yang, B. Chen and H. Zhang, *Chem. Rev.*, 2018, **118**, 6409–6455.
3 N. Baig, *Composites, Part A*, 2023, **165**, 107362.
4 V. Sethumadhavan and Nonappa, *Dalton Trans.*, 2025, **54**, 11770–11789.
5 C. Li, Y. Jin and Q. Shao, *Small*, 2025, **21**, 2505810.
6 Y. Ge, Z. Shi, C. Tan, Y. Chen, H. Cheng, Q. He and H. Zhang, *Chem*, 2020, **6**, 1237–1253.
7 I. Jung, S. Lee, S. Lee, J. Kim, S. Kwon, H. Kim and S. Park, *Chem. Rev.*, 2025, **125**, 7321–7388.
8 F. Feng, S. Han, Q. Lu and Q. Yun, *Energy Mater. Devices*, 2023, **1**, 9370008.
9 Z. Li, L. Zhai, Y. Ge, Z. Huang, Z. Shi, J. Liu, W. Zhai, J. Liang and H. Zhang, *Natl. Sci. Rev.*, 2022, **9**, nwab142.
10 D. Su, Z. Lam, Y. Wang, F. Han, M. Zhang, B. Liu and H. Chen, *Joule*, 2023, **7**, 2568–2582.
11 J. Shi, J. Ma, E. Ma, J. Li, Y. Hu, L. Fan and W. Cai, *Carbon Neutrality*, 2024, **3**, 285–312.
12 D. Sayfiddinov, R. S. Kumar, V. Sakthivel, S. Tamilarasi, A. R. Kim and D. J. Yoo, *J. Power Sources*, 2025, **652**, 237595.
13 D. Sayfiddinov, R. Santhosh Kumar, V. Sakthivel, A. R. Kim, S. K. Kim, J. S. Hyun and D. J. Yoo, *ACS Mater. Lett.*, 2025, **8**, 161–170.
14 R. Arukula, M. Vinothkannan, A. R. Kim and D. J. Yoo, *J. Alloys Compd.*, 2019, **771**, 477–488.
15 K. Ramachandran, M. Vinothkannan, A. R. Kim, S. Ramakrishnan and D. J. Yoo, *Int. J. Hydrogen Energy*, 2019, **44**, 21769–21780.
16 C. Cheng and H. J. Fan, *Nano Today*, 2012, **7**, 327–343.
17 Y. Shin, C. Lee, M.-S. Yang, S. Jeong, D. Kim and T. Kang, *Sci. Rep.*, 2014, **4**, 6119.
18 Y. Zhang, Y. Chen, X. Wang, Y. Feng, Z. Dai, M. Cheng and G. Zhang, *Nat. Commun.*, 2024, **15**, 5172.
19 R. Rizo, A. Ferre-Vilaplana, E. Herrero and J. M. Feliu, *ACS Sustainable Chem. Eng.*, 2023, **11**, 4960–4968.
20 X. Wang, H. Yang, M. Liu, Z. Liu, K. Liu, Z. Mu, Y. Zhang, T. Cheng and C. Gao, *ACS Nano*, 2024, **18**, 18701–18711.
21 Y. Zheng, X. Wang, Y. Kong and Y. Ma, *CrystEngComm*, 2021, **23**, 6454–6469.
22 H. C. Kim, R. K. Pramadewandaru, M. K. Kabiraz, G. A. B. Azizar, H. Wahidah, Y. Kim, S.-U. Lee, H.-J. Chae, S.-I. Choi and J. W. Hong, *ACS Catal.*, 2024, **14**, 3756–3765.
23 R. Zhou, X. Fan, X. Ke, J. Xu, X. Zhao, L. Jia, B. Pan, N. Han, L. Li, X. Liu, J. Luo, H. Lin and Y. Li, *Nano Lett.*, 2021, **21**, 4092–4098.
24 B. Jiang, Y. Guo, F. Sun, S. Wang, Y. Kang, X. Xu, J. Zhao, J. You, M. Eguchi, Y. Yamauchi and H. Li, *ACS Nano*, 2023, **17**, 13017–13043.
25 S. Sun, M. Liu, Y. Mao, F. Liu, X. Xu, Y. Li, X. Lv, S. Zhao, X. Liu, Y. Wu and Y. Chen, *Dalton Trans.*, 2025, **54**, 8306–8316.
26 M. Tsuji, K. Takemura, C. Shiraishi, K. Ikedo, K. Uto, A. Yajima, M. Hattori, Y. Nakashima, K. Fukutomi, K. Tsuruda, T. Daio, T. Tsuji and S. Hata, *J. Phys. Chem. C*, 2015, **119**, 10811–10823.
27 Y. Yang, Y. Wang, Y. Ma, Y. Min and Y. Zheng, *J. Nanopart. Res.*, 2023, **25**, 241.
28 S. Mondal, S. K. De, T. Ghosh, S. Mondal, M. Manna and D. Senapati, *Small Sci.*, 2025, **5**, 2500063.
29 B. Hammer and J. K. Nørskov, in *Advances in Catalysis*, Academic Press, 2000, vol. 45, pp. 71–129.

30 M. D. Segall, J. D. L. Philip, M. J. Probert, C. J. Pickard, P. J. Hasnip, S. J. Clark and M. C. Payne, *J. Phys.:Condens. Matter*, 2002, **14**, 2717.
31 J. P. Perdew, K. Burke and M. Ernzerhof, *Phys. Rev. Lett.*, 1996, **77**, 3865–3868.
32 P. Chettiyankandy, A. Chand, R. Ghosh, S. K. Sarkar, P. Das and S. Chowdhuri, *J. Mol. Liq.*, 2019, **296**, 111820.
33 L. Zhang, K. Lee and J. Zhang, *Electrochim. Acta*, 2007, **52**, 7964–7971.
34 Q. Wu, H. Sun, Y. Min, L. Wang, Z. Wang, Y. Wang, Y. Zhao and Y. Zheng, *CrystEngComm*, 2024, **26**, 5030–5038.
35 D. Xu, X. Liu, H. Lv, Y. Liu, S. Zhao, M. Han, J. Bao, J. He and B. Liu, *Chem. Sci.*, 2018, **9**, 4451–4455.
36 M. R. Langille, M. L. Personick, J. Zhang and C. A. Mirkin, *J. Am. Chem. Soc.*, 2012, **134**, 14542–14554.
37 L. Ma, C. Wang, M. Gong, L. Liao, R. Long, J. Wang, D. Wu, W. Zhong, M. J. Kim, Y. Chen, Y. Xie and Y. Xiong, *ACS Nano*, 2012, **6**, 9797–9806.
38 Z. Chen, J. Zhang, Y. Zhang, Y. Liu, X. Han, C. Zhong, W. Hu and Y. Deng, *Nano Energy*, 2017, **42**, 353–362.
39 M. Liu, M. Xie, Y. Jiang, Z. Liu, Y. Lu, S. Zhang, Z. Zhang, X. Wang, K. Liu, Q. Zhang, T. Cheng and C. Gao, *J. Mater. Chem. A*, 2021, **9**, 15373–15380.
40 L. Chen, L. Lu, H. Zhu, Y. Chen, Y. Huang, Y. Li and L. Wang, *Nat. Commun.*, 2017, **8**, 14136.